Wetting at the Nanoscale

Sylvain Franiatte, Philippe Tordjeman, Thierry Ondarçuhu

Wetting at the nanoscale: molecular mobility induced by contact line forces

Sylvain Franiatte, Philippe Tordjeman, and Thierry Ondarçuhu*

Institut de Mécanique des Fluides de Toulouse (IMFT), Université de Toulouse, CNRS, Toulouse, France

E-mail: thierry.ondarcuhu@imft.fr;philippe.tordjeman@imft.fr

Phone: +33 (0) 534322988

Abstract

In this paper, we study the interaction of a contact line with molecules physically adsorbed on a surface. We developed specific atomic force microscopy (AFM) experiments where a nanoneedle attached at the extremity of the cantilever is dipped in a liquid droplet. The motion of the contact line at the extremity of the meniscus formed depends on the presence of topographical and chemical defects at the surface of the nanoneedle. The analysis of the force measured by AFM based on a capillary model, allows to distinguish the effects of topographical and chemical defects and to monitor minute changes of surface properties. Using six different liquids and five tips, we show that the change of the surface properties of one nanoneedle results from the adsorption of airborne molecules when the tip is left in air and their desorption by the moving contact line. The desorption rate is found to depend only on the number of dipping cycles, and is not influenced by the velocity or the liquid properties. A model based on the estimation of capillary and adsorption energies confirms a capillary desorption mechanism in agreement with the experimental results. Finally, we demonstrate that three distinct desorption mechanisms may be at play. Interestingly, using a deliberate

contamination with large hydrocarbon molecules we show that the capillary desorption studied in this paper can be used to clean surfaces.

Introduction

It is well established that the wetting properties of a sessile drop are fixed by the topographic and chemical properties of the substrate.[1,2] Recently, mechanisms involving the surface modification by a coupling between substrate and liquids have been considered. Substrate surface may adapt to a liquid by minimizing the interfacial energy. This can be achieved by different processes such as chemical groups reorientation, molecular ordering, swelling, diffusion or adsorption...[3] These phenomena are mainly considered at the solid-liquid interface. However, specific interactions can also play at the drop edge[4] and modify the macroscopic wetting behavior. An example of such mechanism is the formation of a ridge on soft solid by elasto-capillarity.[5] The capillary force at the contact line which deforms the solid may also induce local molecular changes and modify the pinning of the sessile drop. The interplay between the substrate modification and the dynamics of the drop is an open question in wetting science, which requires new specific experiments at the molecular scale. The extreme sensitivity of the contact line motion to surface defects leading to contact angle hysteresis has been studied for a long time.[6–8] Both types of defects, topographical and chemical,[9,10] lead to pinning and distortion of the contact line which greatly reduces the spreading and mobility of macroscopic droplets.[11] It was shown that a molecule monolayer[12,13] or an atomic thick coating[14] modifies the wettability of the underlying substrate whereas nanometric asperities can make a surface super-hydrophilic or super-hydrophobic.[15,16] Contamination by particles or chemical species from the liquid or atmosphere also governs the wetting properties in many natural and industrial systems.[17–19] Since molecules adsorption energies and capillary energies are both of the order of a few kT, a possible action of the contact line on the surface, at molecular scale, requires much attention. Though it is known that the capillary force at

the contact line can move particles[20–22] or align DNA[23] or carbon nanotubes,[24] this issue has never been addressed experimentally at the molecular scale.

Atomic force microscopy (AFM) allows to study the dynamics of a nanomeniscus at the nanometer scale.[25–28] Recently, we developed an AFM method which relies on the dipping of nanoneedle attached to an AFM cantilever in a liquid while monitoring the capillary force.[29] In these AFM experiments, the nanoneedle fixed at the extremity of the cantilever is repeatedly dipped in a droplet. The evolution of the capillary force captures minute changes of nanoneedle surface properties. On the basis of this work, we demonstrated that a nanomeniscus which sweeps the needle surface induces the local desorption of molecules and modify the wetting properties of the surface. Interestingly, specific experiments based on partial tip dipping unambiguously demonstrate that the desorption of physically sorbed molecules is induced by the capillary force exerted at the contact line. An important result is that the total removal of contaminants is governed by a characteristic number N^* of dipping cycles which does not depend on velocity and liquid properties.

In the present paper, we detail the interaction of a moving contact line with physically adsorbed species. We first detail the whole experimental results of wetting at the nanoscale. With the help of a model of wetting of a heterogeneous surface, we understand the effects of topographical and chemical defects and show the existence of a molecular desorption mechanism which modifies locally the nanowetting. The change of the surface properties of the nanoneedle by adsorption of contaminants is also considered in the model and verified experimentally. As an application of this work, we demonstrate the efficiency of a moving contact line to clean surfaces at the molecular scale, even in the case of a deliberate contamination.

Experimental section

The experiment is sketched in Fig. 1. An AFM tip ended by a nanoneedle is dipped in and withdrawn from a liquid droplet. This "dipping cycle" is realized at constant velocity V and

the deflection of the cantilever is measured using an AFM. The measured capillary force F is related to the contact angle θ of the liquid on the tip surface through $F = 2\pi R\gamma cos\theta$ where R is the radius of the tip and γ the liquid surface tension.

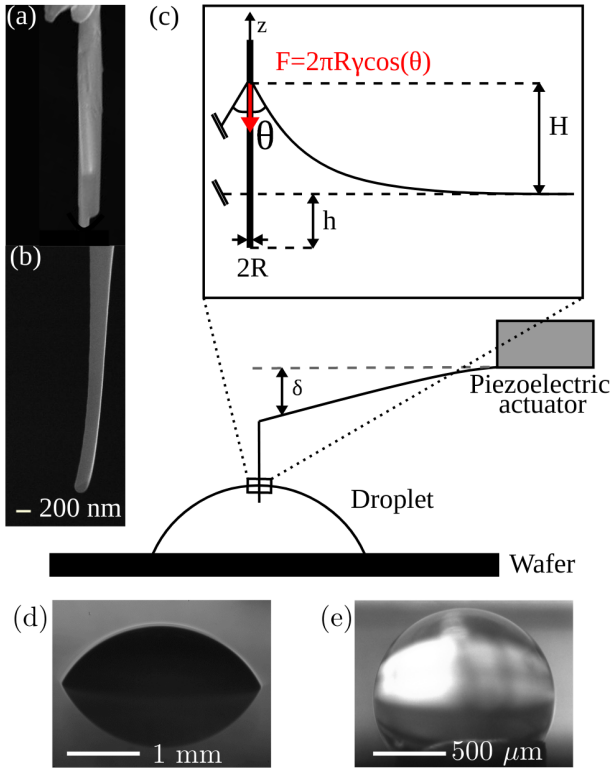

Figure 1: (a)-(b) SEM images of the NN tip and of a nanoneedle fixed at the extremity of the silicon tip, respectively; (c) sketch of the experiment with a zoom on the nanomeniscus for definition of variables; (d) image of a glycerol sessile droplet; (e) image of a water droplet resting at the end of a small capillary connected to a micro-injector.

In this study, we consider six different model fluids, for which the main characteristics are given in the Table 1: ethylene glycol (EG), tetraethylene glycol (4EG), undecanol (Und), hexadecane (Hx), glycerol (Gly) and deionized water (W). Except for water, the liquids are purchased from Sigma-Aldrich (Merck) and are used as received.

Table 1: Relevant properties of the liquids used : volumic mass ρ, viscosity μ, surface tension γ and saturation vapor pressure at 25 °C P_{sat}.

Liquid	ρ (kg/m^3)	μ (mPa.s)	γ(mN/m)	P_{sat} (bar)
Glycerol (Gly)	1260	910	63	0.025
Tetraethylene glycol (4EG)	1120	50	46	7
Ethylene glycol (1EG)	1110	30	50	13
Undecanol (Und)	832	13.8	29	0.4
Hexadecane (Hx)	770	3	27	0.22
Water (W)	997	1	72	3170

The choice of this series of liquids allows us to assess the effects of surface tension, viscosity and saturation vapor pressure. Indeed, among these liquids, the viscosity varies over 3 orders of magnitudes, the vapor pressure over 5 orders of magnitude and the surface tension by a factor of 2.6. Sessile drops of liquids of about 4 mm are deposited on a 1" silicon wafer (Siltronix) cleaned in acetone, isopropanol and water just before AFM experiments (Fig. 1c). In the case of undecanol and hexadecane, the wafer is hydrophobized using 1H,1H,2H,2H, perfluorodecyltrichlorosilane (ABCR, Germany) to avoid the complete spreading of the liquids. Due to evaporation issue which induces a continuous decrease of the liquid height during measurement, droplets of water are produced at the extremity of a teflon capillary connected to a micro-injector (Narishige IM300, Japan) that controls the fluid pressure and therefore the droplet radius (Fig. 1d).

A JPK Nanowizard 3 AFM is operated in contact mode to measure the force curves when a nanoneedle is dipped in a drop at constant velocity comprised between 3 to 200 $\mu m/s$. The cantilever stiffness is characterized by thermal noise using the deflection sensitivity derived from contact mode experiments on a silicon wafer substrate.[30] Note that the stiffness of all cantilevers used ($k \sim 2$ N/m) is at least forty times larger than the effective spring constant of the interface, which is of the order of $\gamma/2$.[31] We record between 4000 and 12000 points for each curve (1 point/nm). The frequency of acquisition of the AFM (200 kHz) is therefore sufficient even for the larger velocity used (200 μm/s). The raw data are analyzed with home-made Python® codes.

Two types of tips are used: commercial NaugaNeedle tip (NN) made in Ag_2Ga alloy (Nauganeedle, USA) and homemade tips (Si1 to Si4) carved at the end of a conventional silicon AFM probe (OLTESPA, Bruker) using a dual beam FIB (1540 XB Cross Beam, Zeiss).[27] The characteristics of the 5 tips used in this study are presented in Table 2. The nanofibers have radius in the range 60-500 nm and length of several microns.

Table 2: Relevant properties of the tips used: quality factor Q, cantilever spring constant k, resonance frequency in air f_0 and radius R.

Pointe	Q	k (N/m)	f_0 (kHz)	R (nm)
Si1	120 ± 3	1.08 ± 0.03	61.7	60 to 125 nm.
Si2	184 ± 11	1.91 ± 0.12	68.2	60 nm
Si3	239 ± 11	3.06 ± 0.14	79.8	70 nm
Si4	197 ± 30	2.13 ± 0.32	70.6	67.5 nm
NN	362 ± 32	3.86 ± 0.34	74.4	310 to 530 nm

All the AFM experiments are realized in a gray room maintained at a constant temperature of 23 ± 1 °C and a relative humidity comprised between 55 and 65 %.

The experiments presented below are based on the measurement of force curves when a nanoneedle is dipped in and withdrawn from the droplet. Figure 2 compares the force curves obtained for a given tip (Si3) and four different liquids. Each curve represents the force F variation as a function of the immersion depth h (see Fig 1) for a same tip velocity $V = 50\mu$m/s. When approaching the interface from above, the tip enters in contact with the liquid at $h = 0$ and the meniscus is formed. As h increases, the contact line advances on the tip surface and the force characterizes the "advancing" branch of the curve. At a given $h \sim 1 - 1.3\mu$m the tip is retracted. In a first step, the force increases linearly while h decreases. In this stage, the contact line is pinned and the contact angle varies from advancing to receding contact angles which induces an increase of capillary force. The negative slope of this branch gives the meniscus stiffness.[31] In a second step, the contact recedes on the tip until it reaches the end and the meniscus breaks. Damped oscillations of the cantilever are observed once the tip is released.

Considering the force curve for glycerol (Fig 2a), we observe that the advancing and

receding curves are characterized by similar features: two large peaks followed by smaller ones are measured in both branches. The fact that we observe the same peaks in the two parts of force curves, which can be linked by a line with a slope equal to the meniscus stiffness, demonstrates that the defects are of topographic nature and not chemical one.[11,27] Some differences between advancing and receding curves may be attribute to asymmetric defects that pin the contact line more strongly in one direction than in another. Hence, the force curve realized with glycerol indicates that the nanoneedle exhibits two "big" topographic defects followed by smaller ones, leading to the contact angle hysteresis. These features appear with all liquids, although the magnitude of the force depends on the surface tension of the liquid and on the contact angle. In particular, for undecanol (Fig 2d), due to the small surface tension of this liquid, advancing and receding curves are nearly superimposed and the two large peaks are smoother (as discussed in ref[26]). Finally, the fact that the same characteristics of the curves remains after thousands of dipping cycles in each liquid is an indication of the cleanliness of the experimental conditions and the robustness of the results.

We realized two types of experiments called I and II. The first one consists of 100 successive dipping cycles at a constant tip velocity in ambient conditions in order to monitor the evolution of the nanoneedle surface properties with the number of cycles N. With that aim, all force curves are recorded and analyzed by plotting the force associated with one peak (one defect) as a function of N. In the second experiment, we perform 10 successive series of 100 dipping cycles separated by various times t_p during which the tip is left in air. Here, we investigate the effects of airborne contaminants and their adsorption dynamics on the tip surface. These two experiments are realized for all the liquids and 5 velocities to understand the mechanism of desorption of airborne molecules induced by a moving contact line.

After proving that airborne molecules are responsible of the nanoneedle contamination, we also developed a specific experiment with a deliberate contamination by exposition of the tip to hexadecane vapor wich is detailed in the Desorption Mechanism section.

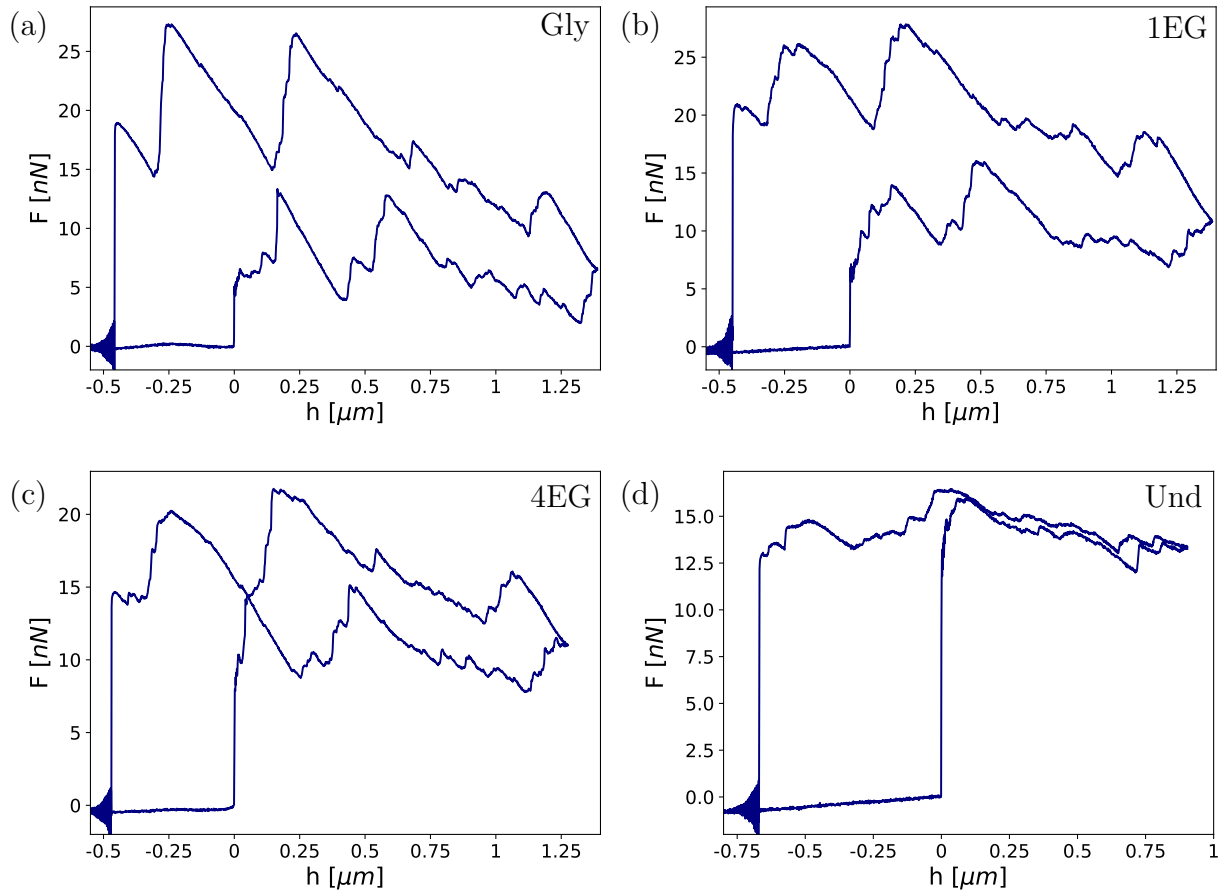

Figure 2: Force curves obtained with the Si3 tip at 50 $\mu m/s$ in glycerol (a), ethylene glycol (b), tetra ethylene glycol (c) and decanol (d).

Capillary force model for a cylinder with topographical defects

The nanoneedle fabrication process always leads to the presence of topographical defects. These defects are responsible for force peaks and hysteresis in the capillary force measurements. Since these nanodefects are difficult to characterize by standard microscopy methods, it is useful to settle our analysis of experimental data on a simple model.

We consider a cylinder along the z axis for which the radius is a function $r(z)$ of the vertical position. This cylinder is partially dipped in a liquid. We note h the distance from the

basis of the cylinder to the flat liquid surface reached beyond the capillary length l_c, and z_{CL} the distance from the contact line to the extremity of the cylinder (see Fig. 1c). The height of the meniscus is given by $H = z_{CL} - h$. In our experiment the capillary force F is measured as a function of the immersion depth h. The model allows to compute $F(h)$ from the following equations:[32] $F = 2\pi\gamma r(z_{CL})\cos(\theta_v(z_{CL}))$, where θ_v is the angle between the liquid interface and the vertical axis z; this angle can be expressed as a function of the constant equilibrium contact angle θ_0 of the liquid on the cylinder, $\theta_v(z_{CL}) = \theta_0 - \arctan r'(z_{CL})$; the height H of the meniscus is given by:[33] $H(z_{CL}) \cong r(z_{CL})\cos\theta_v(z_{CL})\left[\ln\left(\frac{4l_c}{r(z_{CL})(1+\sin\theta_v(z_{CL}))}\right) - C\right]$, where $C \simeq 0.57721$ is the Euler constant. These equations are solved using Python® code for a given $r(z)$. For the sake of simplicity, we use a sine function with small amplitude b and wavelength λ for the small scale roughness and Gaussian functions to mimic i blemishes characterized by an height A_i, a width σ_i at different positions z_i: $r(z) = r_0 + b\ sin(2\pi z/\lambda) + \sum_i A_i \exp[-(z - z_i)^2/2\sigma_i^2]$.

We assessed the validity of this modelling on the curves of Fig. 2 which were obtained for the same tip in four different liquids. As discussed in the previous section, the qualitative analysis of the force curves reported on Fig. 2 allows to infer that the tip surface exhibits 2 large topographical defects, followed by several smaller ones. We therefore define a $r(z)$ with 6 successive defects, 2 large ones and 4 smaller ones modelled by Gaussian functions with $A = 20, 30, 2, 2, 2, 10$ nm and $\sigma = 80, 80, 2, 2, 2, 2$ nm. In addition we superpose a sinusoidal function with amplitude $b = 0.2$ nm and wavelength $\lambda = 5$ nm to mimic the small scale roughness of the tip after fabrication process and a parabolic variation of the radius r_0 with z to reproduce the change in tip section. The force curves computed by the model on such a tip for the four liquids (glycerol, ethyleneglycol, tetra ethyleneglycol, undecanol) used in Fig. 2 are reported in Fig. 3. For each liquid, the value of θ_0 is varied over five degrees to evidence the influence of the contact angle on the force curves.

The comparison of the computed and experimental curves is fairly good, in particular given the fact that the model considers axisymmetric defects, which is probably not the case

for real tips. The overall shape of the curves are reproduced with the 2 large peaks and the smaller ones, with force values close to the experimental ones. The hysteresis between advancing and receding curves is also found to decrease when the contact angle decreases, reaching a very small value for undecanol. The model also predicts well the position of the peaks and the (negative) height h at which the meniscus breaks. This shows that the analysis of the force curves allows a description of the tip surface topography with a nanometric precision. On Fig. 3 are also reported the variation of the force with a small increase of the contact angle θ_0 on the surface (from red to blue). It shows that a decrease of θ_0 leads to an increase of the force on both advancing and receding branches. As expected, the force increase is less pronounced in the part of the curves for which the contact line is pinned on a defect (for example $0 \lesssim h \lesssim 0.5\mu$m in the receding branch). It also leads to a translation of the peaks position along the h axis. This is due to the fact that the meniscus height H varies with θ_0. The measurement of capillary force therefore allows to monitor minute changes of surface properties, in particular for liquids with large surface tensions. For undecanol, due to small contact angles values the variations are much smaller.

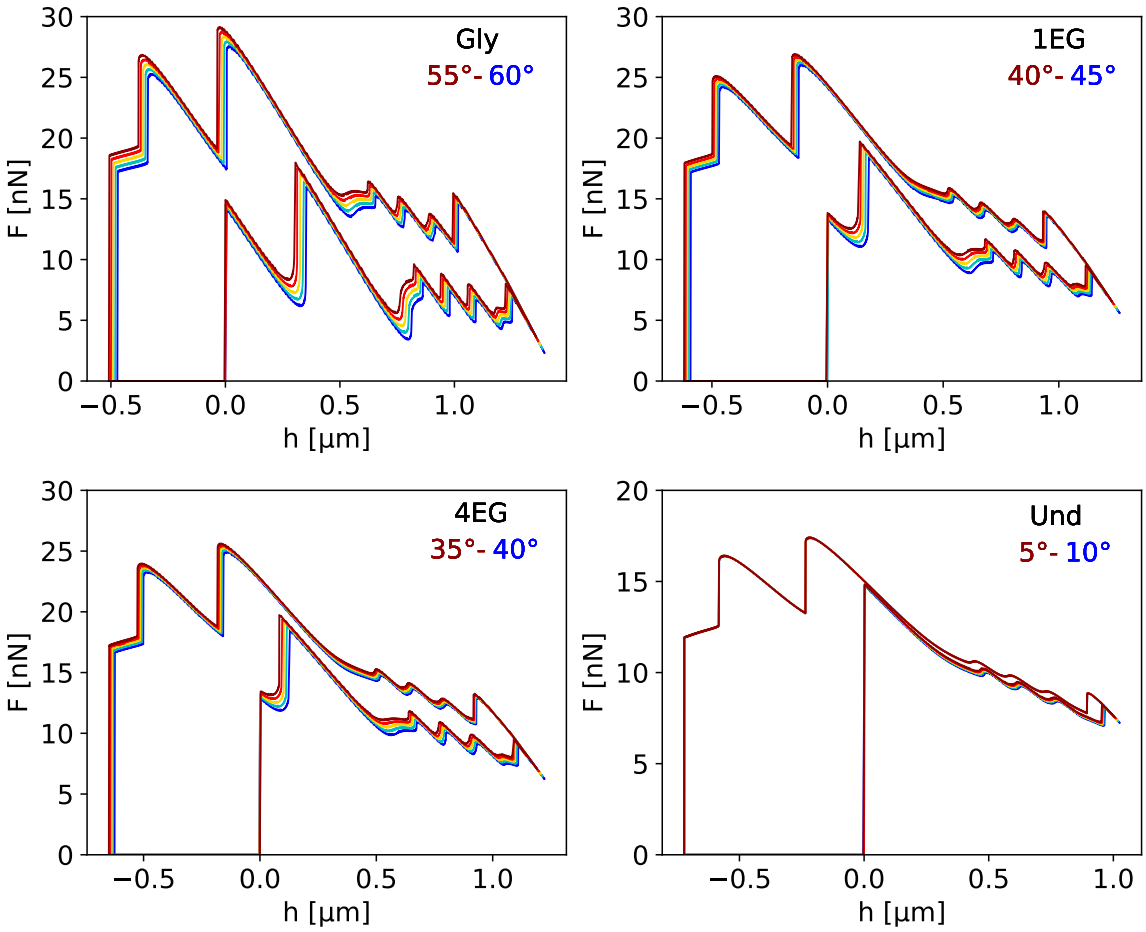

Figure 3: Simulated force curves using the expression of $r(z)$ given in the main text for the tip profile. The liquid name and the range of θ_0 values used in the calculations (decreasing from blue to red) are reported as legends.

Experimental results

In Fig. 4 are plotted the typical results of experiment I (100 successive dipping cycles) for six liquids and tips, at different tip velocities V (see caption). In this representation we selected several force curves at different numbers N of wetting cycles to show the evolution of the tip surface properties. The number N of wetting cycles increases from blue to red force curves. Compared to the initial curve, we observe a global enhancement of the capillary

force both in the advancing and receding branches when N increases, for all liquids except for hexadecane. Interestingly, the details of the advancing and receding curves does not show any evolution which suggests that the observed evolution when N increases is due to a change of the surface energy of the needle without any modification of its topography, as modelled in the previous section (Fig. 3). This fundamental result is general for all liquids (except for hexadecane) and all experimental conditions. On the other hand, the amplitude of change varies with liquid nature and is, in the limit of uncertainties, independent of tip type and V. For hexadecane no measurable evolution is observed.

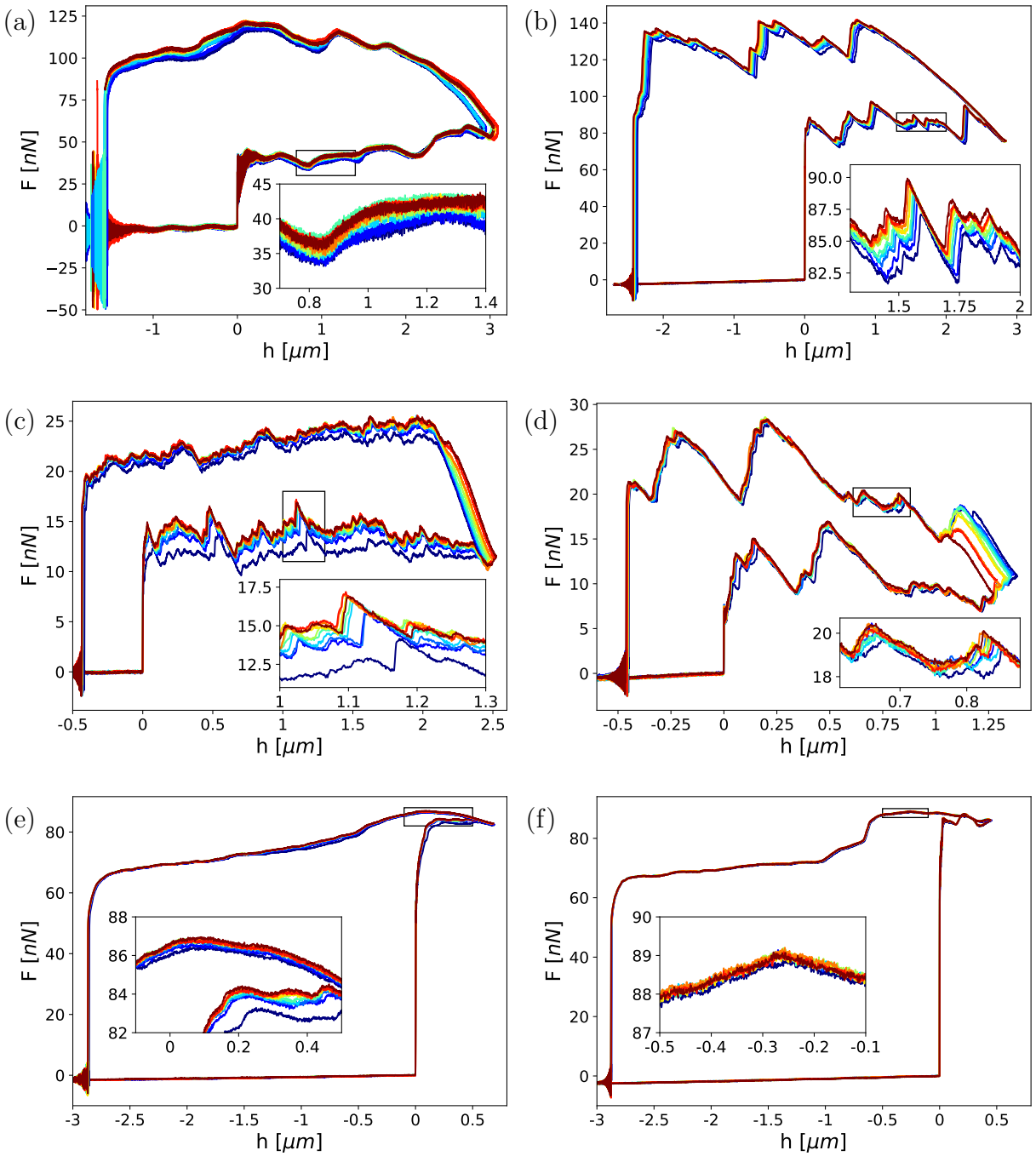

Figure 4: Force curves obtained in water at $V = 200\,\mu m/s$ (a), tetraethylene glycol at $V = 50\,\mu m/s$ (b) (both with the NN tip), glycerol (Si4 tip at 50 $\mu m/s$) (c), ethylene glycol (Si3 tip at 50 $\mu m/s$) (d), undecanol (e) and hexadecane (f) (both obtained with the NN tip at $V = 50\,\mu m/s$).

In order to characterize quantitatively the force variation, we select one defect in the advancing (receding) branch and measure the associated minimum (maximum) force F as a

function of N. Figure 5 represents the relative variation of the force $\Delta F/F_\infty = (F - F_0)/F_\infty$ as a function of N for different liquids and tips, where F_0 and F_∞ are the values of F for $N = 0$ and $N = 100$, respectively. All curves show that the relative force increases and reaches a plateau after about 20 dipping cycles. We also observe that the data obtained with NN tip (Fig. 5b) are more accurate than with Si tips (Fig. 5a). This is due to the larger tip radius of NN (Table 2) which improves the signal-to-noise ratio. The results plotted in logarithmic scale show that the amplitude of the force change strongly depends on the nature of the liquid (typically from 30 % for glycerol and water down to 0.4 % for undecanol). However, the dynamics as a function N seems to be similar.

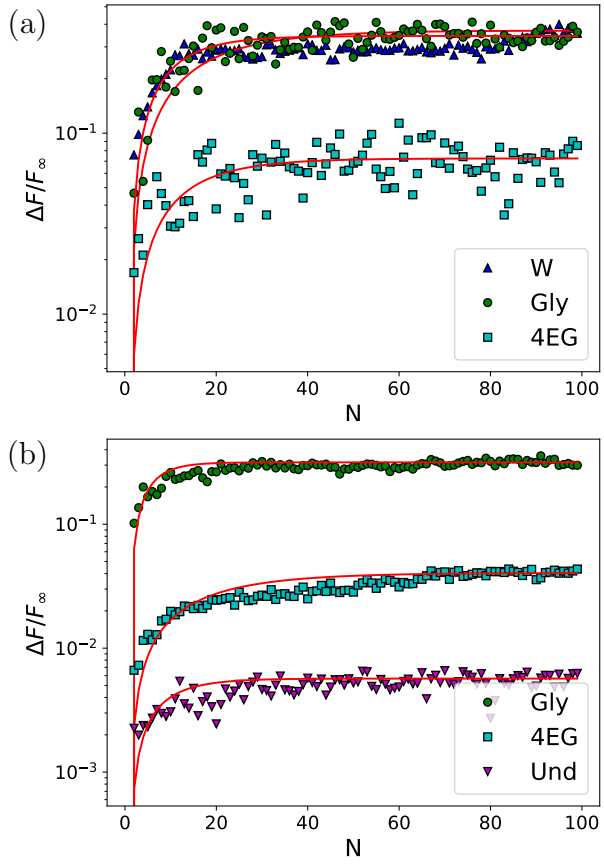

Figure 5: Force variation $\Delta F/F_\infty$ as a function of N for: (a) three different liquids (W, Gly, 4EG) with the Si3 tip at $V = 200\mu$m/s; (b) three different liquids (G, 4EG, Und) with the NN tip at $V = 50\mu$m/s. Red curves are fits of the data with $\Delta F/F_\infty = (1 - F_0/F_\infty)(1 - e^{-N/N^*})$.

The experimental data can be fitted by a simple exponential equation $F = F_\infty + (F_0 -$

$F_\infty)e^{-N/N^*}$ where N^* is the characteristic number of cycles required to reach a stationary force. For all liquids and tips we find $N^* = 14 \pm 5$. This result points out that the physical properties of the liquid does not play any role in the value of N^*. Given the large range of vapor pressures and viscosities for the liquids used (Table 1), this rules out any effect of evaporation or viscous stress on the observed phenomenon. The measurements of N^* at different V also show no clear evolution except at low velocity value, *i.e.* V <25 μm. This point is discussed below.

A typical result of experiment II is presented in Fig. 6. This curve is composed of 12 successive series of experiments I, separated by various contamination times t_p during which the tip is left in air. The values are fixed in order to study the influence of t_p and verify the reproducibility of the experiments. The first series corresponds to an unknown value of t_p since it is the first one after mounting the tip on the cantilever holder. The other series are obtained for t_p values between 1 and 31 s. As expected, for each series we recover the behavior described above with an increase of the force until a plateau F_∞. Figure 6 shows that F_∞ may slightly differ due to the high sensitivity of AFM experiments. However, in the limit of experiments accuracy, we find that the values of F_∞ and N^* are similar for all series. We observe that the values of F_0 decreases significantly with t_p. For short $t_p = 1$ s values, F_0 is close to F_∞. If we compare the results of all series, we check that F_0 is fixed by t_p. Indeed, the second series corresponding to $t_p = 8$ s is characterized by a value comparable to those of 6^{th} ($t_p = 10$ s) and 7^{th} ($t_p = 14$ s) ones.

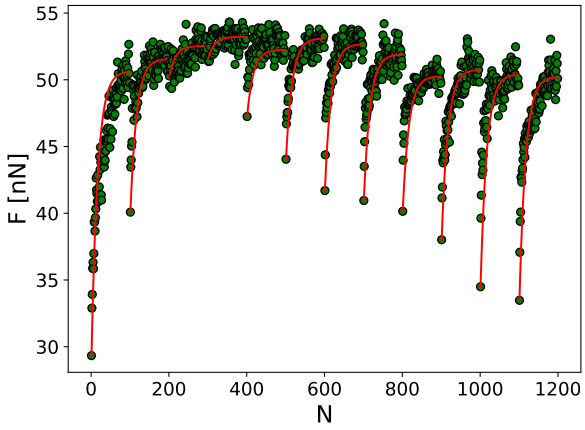

Figure 6: Force F measured on one peak of the advancing branch of the NN tip in Gly at $V = 50\mu$m/s as a function of N for 12 series of 100 dipping cycles. The values of the delay time t_p between series are 8, 1, 1, 6, 10, 14, 16, 17, 21, 25, 31 s, respectively.

Except for hexadecane which does not show any evolution, we plot $\epsilon = \frac{F_\infty - F_0}{F_\infty}$ as a function of t_p for all liquids and velocities. Examples are given in Fig. 7. All the curves follow an exponential function $\epsilon = \epsilon_{max}\left(1 - e^{-t/\tau}\right)$. For all liquids, tips and velocities, we measure a same value $\tau = 7 \pm 4$ s. Conversely, ϵ_{max} varies over 2 orders of magnitude depending on the liquid nature, the lower the surface tension, the lower the amplitude of force change due to contamination.

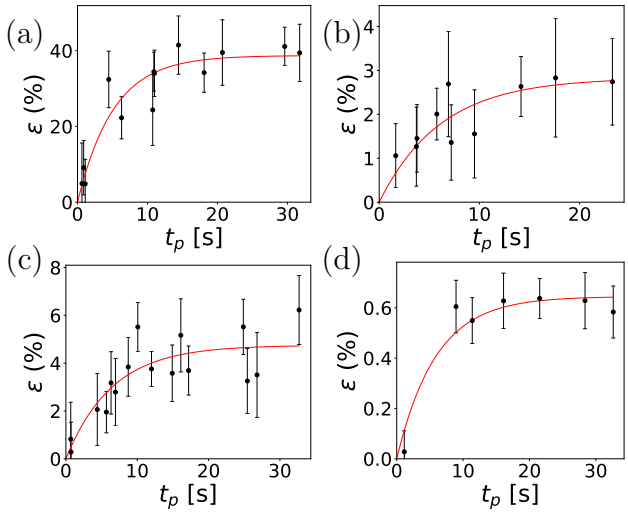

Figure 7: Relative force variation ϵ as a function of contamination time t_p for glycerol with the Si3 tip (a), tetraethylene glycol with the Si3 tip (b), ethylene glycol with the Si3 tip (c) and undecanol with the NN tip (d).

In this work, we realized about 30,000 dipping force curves for each tip. The results for one liquid, one tip and one velocity can be presented by plotting a 3D map $F(h, N)$ which gathers, in color code, all $F(h)$ force curves for all the N dipping cycles. An example of such a map is given in Fig. 8 (left) for the experiment II of Fig. 5. The real interest of this map is to give a comprehensive view of the wetting property evolution for the whole tip (all defects). This map can be understood by plotting on the same figure, the $F(N)$ curve for the topographical defect corresponding to $h \simeq 0.3\mu$m (defect 1). The map displays clearly the series of eight experiments I. We observe that the force variation linked to the change of θ_0 for the topographical defect 1 (Fig 5b) is coupled to a shift in h that results from a change of meniscus height H, as pointed out in the Model section (Fig. 3). Hence, the $F(h, N)$ maps display the evolution of the capillary force with the number of dipping cycles for the whole tip wetted surface. In this representation, the series are clearly identified.

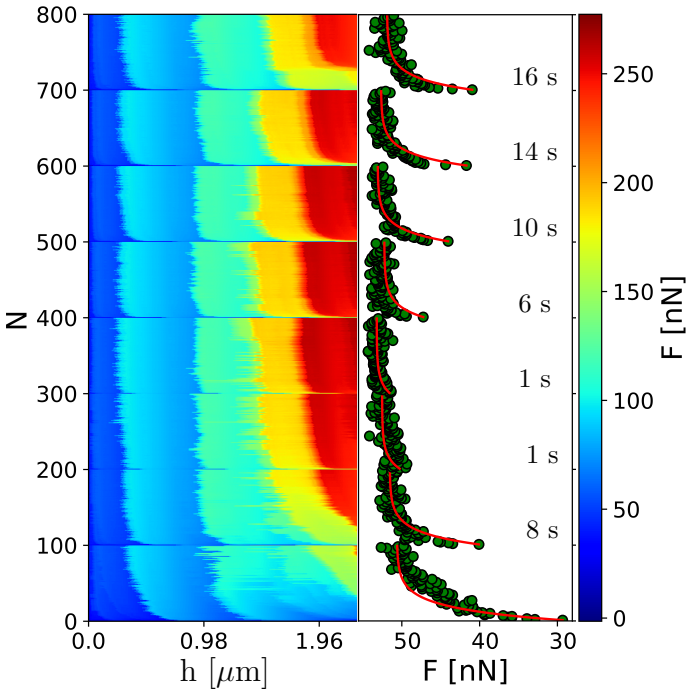

Figure 8: Force F as a function of the height h and the dipping cycle number N at the advancing for the left part of the figure. Force F measured on one peak of the advancing for the right part. These data have been obtained with the NN tip in glycerol at $V = 50\,\mu m/s$, as for Figure 6.

Desorption mechanism

The experiments reported above demonstrate that AFM allows to monitor minutes changes in the wetting properties of a solid surface with a good time resolution. This is possible thanks to a precise understanding of the force curves shape which allows to disentangle the effects of topography and chemistry of the tip. The results based on the analysis of more than 30,000 force curves for each tip show a good reproducibility which allows to draw robust conclusions about the adsorption of airborne contaminants and their desorption by a moving contact line.[29] In this section, we discuss more quantitatively the different mechanisms at play in this processes. Note that we study only the adsorption and desorption of weakly adsorbed contaminants. Chemically bonded molecules may also be present from the beginning and throughout the whole experiments, and are insensitive to capillary forces.

The adsorption stage is characterized by two parameters extracted from the force curves, namely the characteristic adsorption time τ and the relative change of force ϵ_{max} obtained at saturation when the tip is left for a long time in air. As expected, the value of $\tau = 7 \pm 4$ s is independent of the experimental conditions. This value is much shorter than the typical timescale of contamination of surfaces by airborne hydrocarbon molecules which are of the order of tens of minutes.[34] However, a recent study performed on graphite points out that a rapid contamination by strongly adsorbed contaminants occurs just after exfoliation.[35] In Fig. 9, we report the values of ϵ_{max} which greatly increase with the liquid surface tension. For undecanol, the force change is of the order of 0.5 % whereas it reaches more than 30 % for glycerol and water. In order to interpret this result, we assume a surface with contact angle θ_0, partially covered with a surface fraction Φ of hydrophobic molecules characterized by a contact angle θ_d for a full coverage ($\Phi = 1$). Following the approach proposed by Cassie and Baxter,[36] the equilibrium contact angle θ on the composite surface is given by $\cos\theta = \cos\theta_0 + \Phi(\cos\theta_d - \cos\theta_0)$ which leads to a maximum relative force variation $\epsilon_{max} = \Phi_{max}\left(\frac{\cos\theta_0 - \cos\theta_d}{\cos\theta_0}\right)$ where Φ_{max} is the maximum fraction of the tip surface covered by contaminants. The values of θ_0 are extracted from the experiments whereas the values

of θ_d are retrieved from the literature as the contact angle values of the liquid on paraffin which mimics a surface fully covered ($\Phi = 1$) by hydrocarbons,[37–40] assumed as the main contaminants. On Fig. 9 are reported in green the estimated values for all liquids for a value of $\Phi_{max} = 7$ %. It reproduces fairly well the large range of evolution of contact angle as a function of the liquid nature. The value of Φ_{max} corresponds to a maximum coverage of one molecule per nm^2 if we assume short hydrocarbon chain molecules.[41] This is comparable with the density of single silanol groups[42] which may play as adsorption sites. This calculation allows to estimate the characteristic distance between molecules $\xi \simeq 1$ nm which will be used in the model.

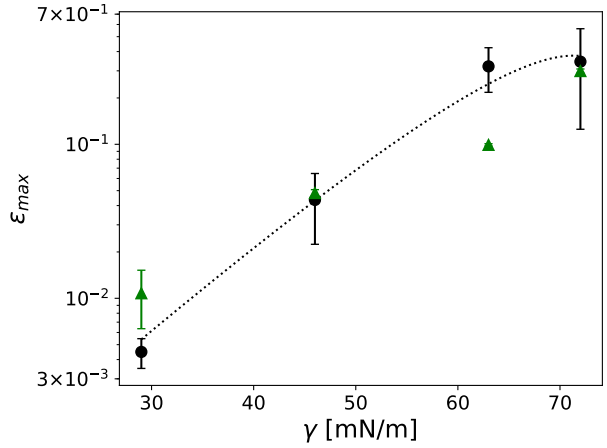

Figure 9: ϵ_{max} as a function of surface tension γ. The round black points are obtained with our data and their error bars refer to statistical uncertainties (95% of confidence). The triangular green points are obtained thanks to the literature data and their error bars refer to the uncertainties given in the literature and an uncertainty of 5° on the results of our contact angle calculation.

The experiments I allow to demonstrate that the continuous sweeping of a surface by the contact line is able to desorb locally contaminant molecules. This process is quantified by the characteristic number of cycles needed to remove these molecules and recover a clean surface. The contaminant surface coverage Φ defined above follows the relationship $\Phi = \Phi_{max} e^{-\frac{N}{N^*}}$. Interestingly, the value of N^* is found to be independent of the liquid used (except for hexadecane for which no evolution is observed). We plot in Fig. 10, the average value of N^* for all tips and liquids as a function of the tip velocity V. No evolution is clearly observed

except a small decrease for small velocities, leading to a value $N^* = 14 \pm 5$ independent of experimental conditions. This rules out any temporal process, such as a diffusive desorption of the molecules in the liquid or any action of viscous stress (in particular at the contact line) that would lead to a velocity dependence. Moreover, the value of the capillary number in our experimental conditions $Ca = \eta V/\gamma \sim 10^{-4} - 10^{-8}$ confirms the fact that capillary effects at the contact line are predominant in the desorption mechanism. The decrease of N^* for small V values can be attributed to recontamination. To evaluate this effect, we estimate the time T spent by the tip in air between two cycles. It is of the order of $T = L_a/V$ where L_a, the average length of the cycle during which the tip is in air, is of the order of $L_a \sim 1 - 3\mu$m. For large velocities, the time T is very short compared to the adsorption time τ leading to a constant desorption rate with no possibility of contaminant adsorption but it becomes comparable for small velocities. Two antagonistic effects are then at play, pure desorption characterized by N^∞ and adsorption characterized by T/τ. Assuming exponential evolution for both mechanisms, we get:

$$\Phi = \Phi_{max}\left(1 - \frac{1 - e^{-1/N^\infty}}{e^{T/\tau} - e^{-1/N^\infty}}\left(1 - e^{-N\left(\frac{1}{N^\infty} + \frac{T}{\tau}\right)}\right)\right), \tag{1}$$

which defines an effective number of cycles given by:

$$\frac{1}{N^*} = \frac{1}{N^\infty} + \frac{L_a}{V\tau}. \tag{2}$$

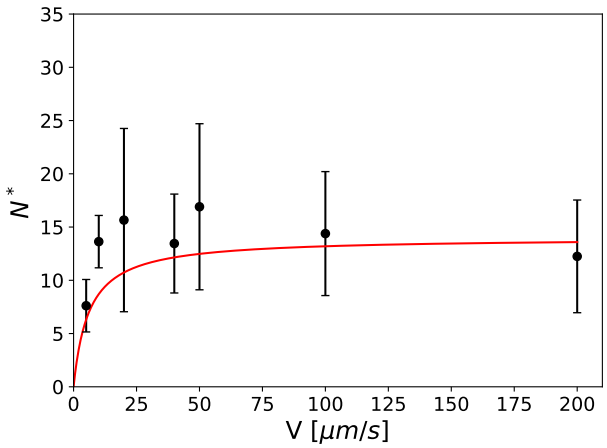

Figure 10: N^* vs. V measured experimentally. The error bars refer to the standard deviations of the measurements. The red curve is a plot of the N^* vs. V from Eq. 2 which takes into account the kinetics of contamination.

We plot on Fig. 10, in red solid line, the result of Eq. 10 with $\tau = 7$ s, $N^\infty = 16$ and $L_a = 3\mu$m. The overall evolution is well described and validates the fact that the decrease of N^* at small velocity is due to a recontamination effect. If we neglect this effect, an intriguing results of our experiments is that the desorption of molecules is governed by the number of times the contact line sweeps the solid surface. Again considering the contaminant molecules as short hydrocarbon chains (propane, butane), their adsorption energy on a silica surface is of the order of $E_{ads} \sim 10kT$.[43,44] This energy barrier which prevents a desorption by thermal energy can be decreased by the capillary energy E_{cap}. This quantity can be estimated by considering the elastic energy stored in the deformation of a contact line caused by the presence of contaminant molecules. According to[11] , these weak heterogeneities leads to a capillary energy per molecule given by $E_{cap} = \gamma\xi^2 \left(\frac{\cos\theta_d - \cos\theta_0}{2\theta_0}\right)^2 \times \ln\left(\frac{L}{\xi}\right)$, where $\xi \sim 1\,nm$ is the distance between molecules as deduced above and L is the tip perimeter. As reported in[29] , the value of E_{cap} is of the order of $7 - 7.5kT$ for all liquids. This value is comparable to contaminants physical adsorption energy and may therefore lower the desorption energy barrier. On the contrary, it is not sufficient to remove molecules chemically adsorbed on the surface (with energies of the order of 100 kT).

While the velocity does not affect the desorption mechanism characterized by a constant

N^* value, the tip velocity governs the dynamics of the contact line. In our experimental conditions where $Ca = \eta V/\gamma \sim 10^{-4} - 10^{-8}$, viscous dissipation is negligible. However, non linear effects arise from the pinning of the contact line on topographical and chemical defects through thermally activated processes.[45,46] The model presented above that computes the static angle θ_v when the contact line moves on a topographical defect allows to simulate the experimental force curve. This model is purely deterministic and depends simply on the equilibrium contact angle θ_0. Our experiments show that the molecular mobility affects θ_0, through adsorption/desorption mechanisms. Yet, θ_0 also depends on the dipping velocity. Figure 11 displays the velocity dependence of the capillary force in a semi-log representation. The data are obtained by repeating experiment I for dipping velocities comprised between 3 and 200 μm/s. The curve compares the force F_0 obtained on the first cycle for each velocity, on one topographical defect, and F_∞ averaged over the last 10 cycles of the series. As an example, the inset of Fig. 11 show the advancing force curve for 6 different velocities at $N = 90$. These data can be interpreted on the basis of a simple kinetics model[45] where the "jump" contact line frequency on a distance characteristic of surface defects λ depends on the contact line force F as: $\nu = \nu_0 \exp\left[-(E_0 - \lambda\Delta F)/kT\right]$ where E_0 is the energy barrier height, ν_0 the attempt frequency characteristic of the liquid and $\Delta F = F(V) - F(V = 0)$ which is negative when the contact line advances. Considering that $V \simeq \nu\lambda$, the force dependence on velocity is given by $\Delta F = \frac{n}{\lambda}[kT \ln(V/V_0) + E_0]$ where $n = 2\pi R/\lambda$ is the number of defects on the needle perimeter.

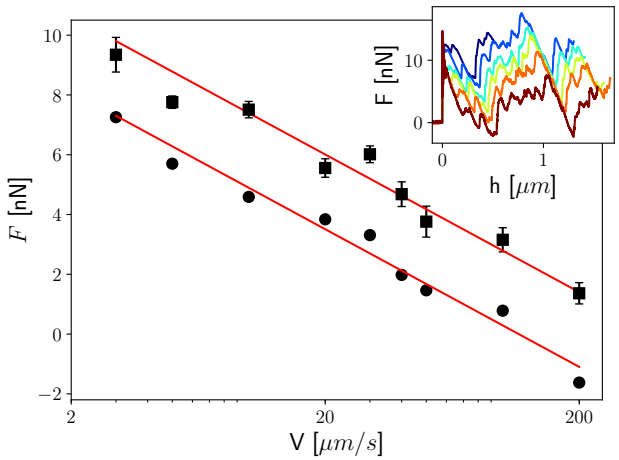

Figure 11: Force F measured on one peak of the advancing branch of the Si1 tip in Gly as a function of the velocity V. The round points are the first measures of a 100 dipping cycles series for each velocity. The square points are the means of the last ten measures and the error bars associated refer to the statistical uncertainties (95% of confidence). Red curves are logarithmic with a slope of 4.6. The inset shows the forces measured on the advancing branch at different velocity from refers to $V = 3\,\mu m/s$ (blue curve) to $V = 200\,\mu m/s$) (brown curve).

The experimental $F(V)$ curves (Fig. 11) follow a logarithmic trend, in good agreement with the model. In particular, we note that the curves for F_0 and F_∞ have the same slope nkT/λ. The value of λ extracted from the slope $\lambda \simeq 1.1$ nm which is similar to ξ calculated independently from the value of Φ_{max}. However, the similar slopes of the $F_0(V)$ and $F_\infty(V)$ indicate that the ratio n/λ is constant and is therefore not affected by the desorption mechanism. Thus, contaminant molecules are not the main source of dissipation. On the other hand, they change in the model the barrier height E_0. Note that λ value is also of the same order of magnitude as the small scale roughness scale used in the topographical model.

In order to get more insight on the desorption mechanism, we analysed the $F(h, N)$ maps which allow following the evolution of the whole tip surface upon continuous dipping. The analysis of the whole set of data evidences three main mechanisms associated to the molecular desorption by the moving contact line:

- the sweeping of the tip by the contact line induces a global change of contact angle by

a progressive desorption of contaminants (Fig. 8) on the whole surface of the tip as discussed above.

- a bistable behavior is sometimes observed when the contact line passes a particular topographical defect (Fig. 12 at $h \simeq 0.18\mu$m). In this case, the depinning force alternates randomly between two close values as N increases. The force curves associated with the two states are reported in Fig. 12(a-c). It shows that the depinning of the contact line can occur at two well defined positions. Interestingly, the probability of occurrence of these two states evolves with N: for small N values, the "weak" pinning site is preferred [Fig. 12(c)] and progressively, as N increases, the two sites are equiprobable [Fig. 12(b)] and finally the "strong" pinning site becomes predominant [Fig. 12(a)]. The intermittency then disappears after about 1000 cycles. This bistable dynamics is linked to a local change of wettability at the depinning point when the contact line recedes. One possibility to explain the bistability is to consider that a contaminant can oscillate in position around the depinning point and is finally desorbed.

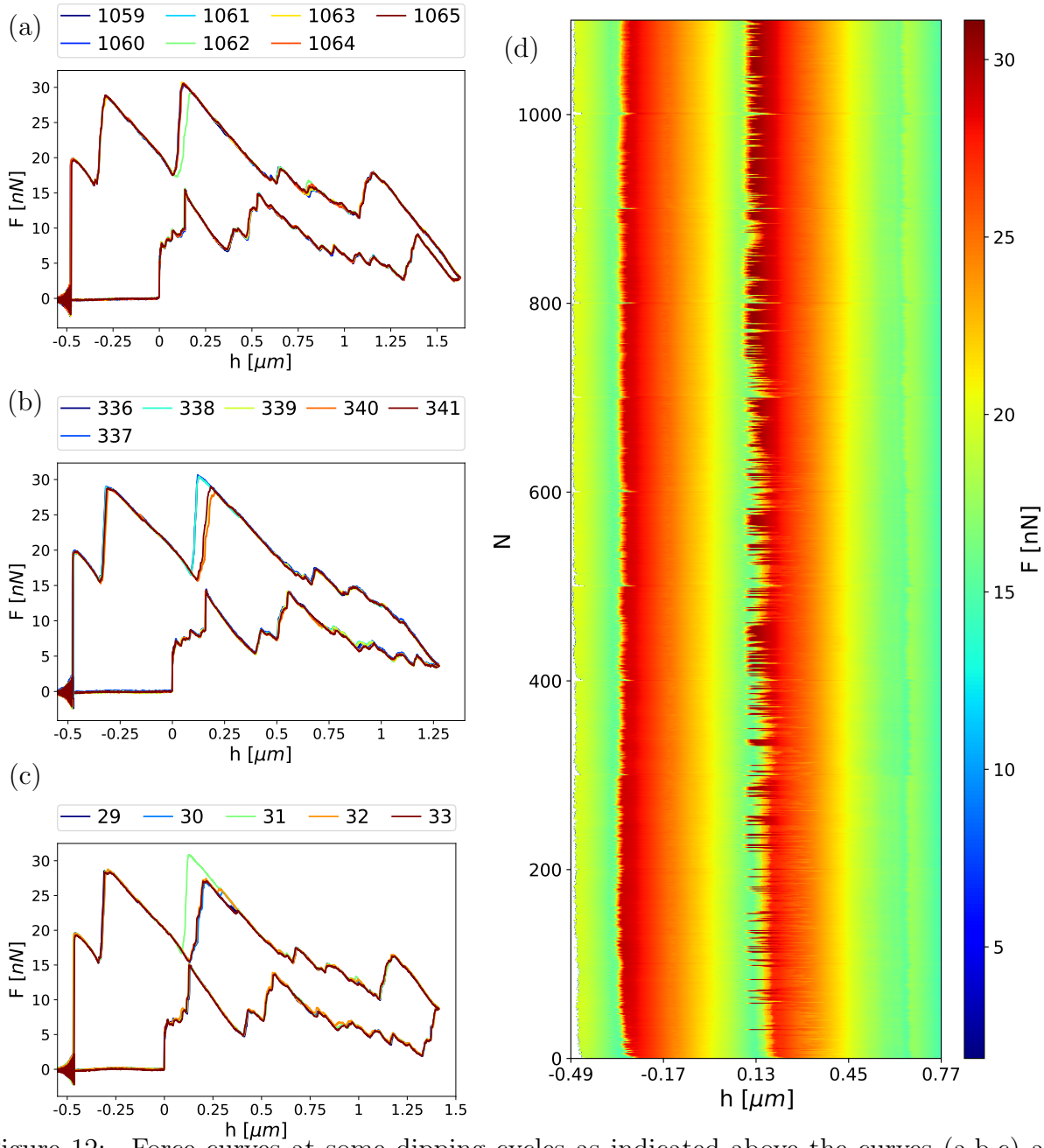

Figure 12: Force curves at some dipping cycles as indicated above the curves (a,b,c) and force F as a function of the height h and the dipping cycle number N at the receding (d). These data have been obtained with the Si3 tip in glycerol at velocity $V = 50\,\mu m/s$.

- a specific experiment of deliberate contamination was achieved by exposing the tip Si4 to a vapor of hexadecane by letting it a few microns above a hexadecane droplet overnight. The map corresponding to 10,000 dipping cycles (experiment I) in glycerol at 50μm/s is reported in Fig. 13. We observe a same trend of force evolution $F(N)$

as previously described. Yet, the force increases over a much larger number of cycles ($N^* \simeq 500$) which is associated with an important level of contamination with large molecules (hexadecane). In this case, the map shows a particular behavior characterized by sudden increase or decrease of force, along topographical defect lines. These large changes in force value may be attributed to the appearance and removal of contaminant clusters which are formed by accumulation of hexadecane on defects by the moving contact line. Example of such clusters are pointed out by arrows on the map of Fig.13. Note that, when left in air, the clean surface obtained at the end of this process is recontaminated by airborne molecules which leads to a $N^* \simeq 15$ value similar with the one obtained in the studies above (not shown). This is consistent with the fact that main volatile organic compounds in air are short hydrocarbon chains. Yet, the particular case of hexadecane contamination clearly demonstrates the efficiency of capillary desorption induced by a meniscus even for large molecules.

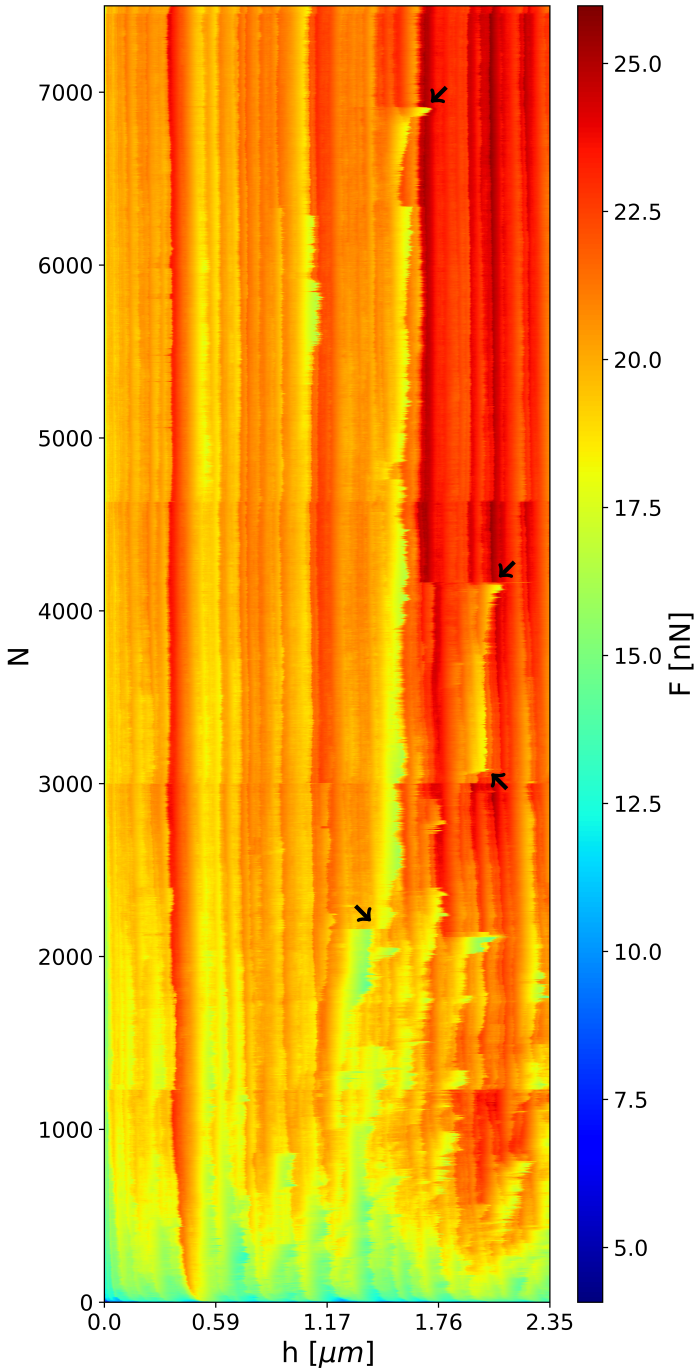

Figure 13: Force F as a function of the height h and the dipping cycle number N at the advancing obtained with the Si4 tip in glycerol at velocity $V = 50\,\mu m/s$.

Conclusions

We developed AFM experiments in order to study the effect of blemishes on the wetting properties of a needle at the nanoscale. We realized about 30,000 dipping cycles per tip at different velocities with 6 liquids with a large range of properties. We obtained very robust results which show that a moving contact line is able to desorb contaminant molecules physically adsorbed on the surface. In our experiments, the adsorption energy of contaminants and the capillary energy are of the same order of magnitude. Two types of experiments permit to characterize both the adsorption and desorption of molecules. In our experimental conditions, we measure a contamination time of the order of $\tau = 7 \pm 4$ s, much shorter than the one observed in the literature. The desorption is characterized by a constant number of dipping cycles N^* independent of velocity and liquid properties but influenced by the nature of contaminants. We identified three mechanisms of desorption: one for which the contaminant molecules are simply swept by the moving contact line; a second for which the molecules are trapped and oscillate in position at the top of a topographical defect; and a third for which molecules of contaminants form clusters which are displaced by the moving contact line.

All the experimental results are analyzed on the basis of a topographical model which allows us to disentangle the contributions of topographical and chemical defects. The AFM experiments at different velocity show that a thermally activated kinetic mechanism governs the dynamics of the contact line at the nanoscale. According to the kinetic model, the change of the surface energy by contaminant desorption modifies the apparent potential barrier. Before or after the decontamination, the dissipation processes occur at the scale of 1 nm and limit the contact line dynamics on the rough surface. One evident application of this work is based in the development of cleaning method by capillary force when clean surface at the molecular scale are required. The patterning of surface at the molecular level could also be achieved by controlling the dynamics of a moving contact line.

References

(1) De Gennes, P.-G. Wetting: statics and dynamics. *Rev. Mod. Phys.* **1985**, *57*, 827.

(2) Bonn, D.; Eggers, J.; Indekeu, J.; Meunier, J.; Rolley, E. Wetting and spreading. *Rev. Mod. Phys.* **2009**, *81*, 739.

(3) Butt, H.-J.; Berger, R.; Steffen, W.; Vollmer, D.; Weber, S. A. Adaptive wetting—adaptation in wetting. *Langmuir* **2018**, *34*, 11292–11304.

(4) Tadmor, R. Open Problems in Wetting Phenomena: Pinning Retention Forces. *Langmuir* **2021**, *37*, 6357–6372.

(5) Andreotti, B.; Snoeijer, J. H. Statics and dynamics of soft wetting. *Annual review of fluid mechanics* **2020**, *52*, 285–308.

(6) Ramos, S.; Charlaix, E.; Benyagoub, A. Contact angle hysteresis on nano-structured surfaces. *Surf. Sci.* **2003**, *540*, 355–362.

(7) Ramiasa, M.; Ralston, J.; Fetzer, R.; Sedev, R. The influence of topography on dynamic wetting. *Adv. Colloid Interf. Sci.* **2014**, *206*, 275–293.

(8) Perrin, H.; Lhermerout, R.; Davitt, K.; Rolley, E.; Andreotti, B. Defects at the nanoscale impact contact line motion at all scales. *Phys. Rev. Lett.* **2016**, *116*, 184502.

(9) Quéré, D. Wetting and roughness. *Annu. Rev. Mater. Res.* **2008**, *38*, 71–99.

(10) Kwok, D. Y.; Neumann, A. W. Contact angle measurement and contact angle interpretation. *Adv. Colloid Interf. Sci.* **1999**, *81*, 167–249.

(11) Joanny, J. F.; de Gennes, P. G. A model for contact angle hysteresis. *J. Chem. Phys.* **1984**, *81*, 552–562.

(12) Silberzan, P.; Leger, L.; Ausserre, D.; Benattar, J. Silanation of silica surfaces. A new method of constructing pure or mixed monolayers. *Langmuir* **1991**, *7*, 1647–1651.

(13) Lim, S. C.; Kim, S. H.; Lee, J. H.; Kim, M. K.; Zyung, T., et al. Surface-treatment effects on organic thin-film transistors. *Synthetic Metals* **2005**, *148*, 75–79.

(14) Ondarçuhu, T.; Thomas, V.; Nunez, M.; Dujardin, E.; Rahman, A.; Black, C. T.; Checco, A. Wettability of partially suspended graphene. *Sci. Rep.* **2016**, *6*, 24237.

(15) Checco, A.; Rahman, A.; Black, C. T. Robust superhydrophobicity in large-area nanostructured surfaces defined by block-copolymer self assembly. *Adv. Mat.* **2014**, *26*, 886–891.

(16) Yuan, J.; Liu, X.; Akbulut, O.; Hu, J.; Suib, S. kong, J.; Stellacci, F. *Nat. Nanotechnol* **2008**, *3*, 332–336.

(17) Okorn-Schmidt, H. F.; Holsteyns, F.; Lippert, A.; Mui, D.; Kawaguchi, M.; Lechner, C.; Frommhold, P. E.; Nowak, T.; Reuter, F.; Piqué, M. B., et al. Particle cleaning technologies to meet advanced semiconductor device process requirements. *ECS J. S. State Sci. Technol.* **2013**, *3*, N3069.

(18) Li, Z.; Wang, Y.; Kozbial, A.; Shenoy, G.; Zhou, F.; McGinley, R.; Ireland, P.; Morganstein, B.; Kunkel, A.; Surwade, S. P., et al. Effect of airborne contaminants on the wettability of supported graphene and graphite. *Nature Mat.* **2013**, *12*, 925–931.

(19) Forrest, E.; Schulze, R.; Liu, C.; Dombrowski, D. Influence of surface contamination on the wettability of heat transfer surfaces. *International Journal of Heat and Mass Transfer* **2015**, *91*, 311–317.

(20) Sharma, P.; Flury, M.; Zhou, J. Detachment of colloids from a solid surface by a moving air–water interface. *J. Colloid Interf. Sci.* **2008**, *326*, 143–150.

(21) Aramrak, S.; Flury, M.; Harsh, J. B. Detachment of deposited colloids by advancing and receding air–water interfaces. *Langmuir* **2011**, *27*, 9985–9993.

(22) Naga, A.; Kaltbeitzel, A.; Wong, W. S.; Hauer, L.; Butt, H.-J.; Vollmer, D. How a water drop removes a particle from a hydrophobic surface. *Soft Matt.* **2021**, *17*, 1746–1755.

(23) Bensimon, D.; Simon, A. J.; Croquette, V.; Bensimon, A. Stretching DNA with a Receding Meniscus: Experiments and Models. *Phys. Rev. Lett.* **1995**, *74*, 4754–4757.

(24) Gerdes, S.,; Ondarçuhu, T.,; Cholet, S.,; Joachim, C., Combing a carbon nanotube on a flat metal-insulator-metal nanojunction. *Europhys. Lett.* **1999**, *48*, 292–298.

(25) Yazdanpanah, M. M.; Hosseini, M.; Pabba, S.; Berry, S. M.; Dobrokhotov, V. V.; Safir, A.; Keynton, R. S.; Cohn, R. W. Micro-Wilhelmy and related liquid property measurements using constant-diameter nanoneedle-tipped atomic force microscope probes. *Langmuir* **2008**, *24*, 13753–13764.

(26) Delmas, M.; Monthioux, M.; Ondarçuhu, T. Contact angle hysteresis at the nanometer scale. *Phys. Rev. Lett.* **2011**, *106*, 136102.

(27) Mortagne, C.; Lippera, K.; Tordjeman, P.; Benzaquen, M.; Ondarçuhu, T. Dynamics of anchored oscillating nanomenisci. *Phys. Rev. Fluid* **2017**, *2*, 102201.

(28) Guo, S.; Gao, M.; Xiong, X.; Wang, Y. J.; Wang, X.; Sheng, P.; Tong, P. Direct measurement of friction of a fluctuating contact line. *Phys. Rev. Lett.* **2013**, *111*, 026101.

(29) Franiatte, S.; Tordjeman, P.; Ondarçuhu, T. Molecular Desorption by a Moving Contact Line. *Physical Review Letters* **2021**, *127*, 065501.

(30) Burnham, N.; Chen, X.; Hodges, C.; Matei, G.; Thoreson, E.; Roberts, C.; Davies, M.; Tendler, S. Comparison of calibration methods for atomic-force microscopy cantilevers. *Nanotechnology* **2002**, *14*, 1.

(31) Dupré de Baubigny, J.; Benzaquen, M.; Fabié, L.; Delmas, M.; Aimé, J.-P.; Legros, M.; Ondarçuhu, T. Shape and effective spring constant of liquid interfaces probed at the nanometer scale: Finite size effects. *Langmuir* **2015**, *31*, 9790–9798.

(32) Fuentes, C.; Hatipogullari, M.; Van Hoof, S.; Vitry, Y.; Dehaeck, S.; Du Bois, V.; Lambert, P.; Colinet, P.; Seveno, D.; Van Vuure, A. W. Contact line stick-slip motion and meniscus evolution on micrometer-size wavy fibres. *Journal of Colloid and Interface Science* **2019**, *540*, 544–553.

(33) James, D. F. The meniscus on the outside of a small circular cylinder. *Journal of Fluid Mechanics* **1974**, *63*, 657–664.

(34) Li, Z.; Wang, Y.; Kozbial, A.; Shenoy, G.; Zhou, F.; McGinley, R.; Ireland, P.; Morganstein, B.; Kunkel, A.; Surwade, S. P., et al. Effect of airborne contaminants on the wettability of supported graphene and graphite. *Nature Materials* **2013**, *12*, 925–931.

(35) Salim, M.; Hurst, J.; Montgomery, M.; Tolman, N.; Liu, H. Airborne contamination of graphite as analyzed by ultra-violet photoelectron spectroscopy. *Journal of Electron Spectroscopy and Related Phenomena* **2019**, *235*, 8–15.

(36) Cassie, A.; Baxter, S. Wettability of porous surfaces. *Transactions of the Faraday society* **1944**, *40*, 546–551.

(37) Kamusewitz, H.; Possart, W.; Paul, D. The relation between Young's equilibrium contact angle and the hysteresis on rough paraffin wax surfaces. *Colloids and Surfaces A: Physicochemical and Engineering Aspects* **1999**, *156*, 271–279.

(38) Jańczuk, B.; Białopiotrowicz, T.; Zdziennicka, A. Some remarks on the components of the liquid surface free energy. *Journal of Colloid and Interface Science* **1999**, *211*, 96–103.

(39) Shepard, J.; Bartell, F. Surface roughness as related to hysteresis of contact angles. III. The Systems paraffin–ethylene glycol–air, paraffin–methyl cellosolve–air and paraffin–methanol–air. *The Journal of Physical Chemistry* **1953**, *57*, 458–463.

(40) Good, W. R. A comparison of contact angle interpretations. *Journal of Colloid and Interface Science* **1973**, *44*, 63–71.

(41) Millet, D. B.; Donahue, N. M.; Pandis, S. N.; Polidori, A.; Stanier, C. O.; Turpin, B. J.; Goldstein, A. H. Atmospheric volatile organic compound measurements during the Pittsburgh Air Quality Study: Results, interpretation, and quantification of primary and secondary contributions. *Journal of Geophysical Research: Atmospheres* **2005**, *110*, D07S07.

(42) Nawrocki, J. Silica surface controversies, strong adsorption sites, their blockage and removal. Part I. *Chromatographia* **1991**, *31*, 177–192.

(43) Funk, S.; Goering, J.; Burghaus, U. Adsorption kinetics and dynamics of small organic molecules on a silica wafer: Butane, pentane, nonane, thiophene, and methanol adsorption on SiO2/Si(111). *Appl. Surf. Sci.* **2008**, *254*, 5271 – 5275.

(44) Zhao, Y.; Shen, Y.; Bai, L.; Ni, S. Carbon dioxide adsorption on polyacrylamide-impregnated silica gel and breakthrough modeling. *Appl. Surf. Sci.* **2012**, *261*, 708–716.

(45) Blake, T.; Haynes, J. Kinetics of liquidliquid displacement. *Journal of Colloid and Interface Science* **1969**, *30*, 421–423.

(46) Guan, D.; Wang, Y. J.; Charlaix, E.; Tong, P. Asymmetric and speed-dependent capillary force hysteresis and relaxation of a suddenly stopped moving contact line. *Physical Review Letters* **2016**, *116*, 066102.

TOC Graphic